Impact of processing parameters on mechanical properties of additively manufactured Ti-based BMGs

Hanna Schönrath[1] *Jan* Wegner[1,2], *Martin A.* Schroer[2,3], *Maximilian* Frey[4], *Lars* Bruckhaus[1], *Ralf* Busch[4], *Stefan* Kleszczynski[1,2]

[1] Chair of Manufacturing Technology, Faculty of Engineering, University of Duisburg-Essen, Germany
[2]CENIDE, Center for Nanointegration Duisburg-Essen, University of Duisburg-Essen, Germany
[3]Nanoparticle Process Technology (NPPT), Faculty of Engineering, University of Duisburg-Essen, Germany
[4]Chair of Metallic Materials, Saarland University, Germany

Abstract. Additively manufactured bulk metallic glasses (BMGs) are promising materials for demanding use cases. They feature high strength, elasticity and corrosion resistance. The intrinsic high cooling rates of powder bed fusion (PBF-LB/M) allow for the processing of partially amorphous bulk geometries with variable crystalline material fractions, for which a microstructure-induced increase in hardness is reported in this work. The influence of varying laser power and scan speed on crystallinity, hardness, and density, as measured by X-ray diffraction (XRD), Vickers hardness, and optical density determination, is presented for a Ti-based BMG with the composition $Ti_{60}Zr_{15}Cu_{17}S_8$. It is demonstrated that the hardness increases to 353 HV5 at a normalized energy input of E_0^*=3 with a relative density of >99.95% and a maximized amorphicity.

1 Introduction

Additive manufacturing (AM) has emerged as a promising technique for fabricating complex components with tailored properties, e.g. by inducing desired microstructural orientations or processing novel materials [1,2]. The powder bed fusion laser beam melting of metals (PBF-LB/M) is an AM process that offers the unique potential to manufacture metastable materials [3], such as bulk metallic glasses (BMGs), by vector- and layer-wise addition of material. Each individual weld track experiences cooling rates of up to 10^6 K/s [4], which theoretically promotes the vitrification of a wide range of glass forming alloys to an amorphous microstructure. BMGs exhibit a high elastic limit of up to 2% and a fracture strength of 4 GPa combined with beneficial attributes, such as biocompatibility and stable cryogenic properties [5]. Due to these properties, they are desired materials for applications in medical and electrotechnical devices [5–7]. PBF-LB/M allows overcoming geometrical restrictions imposed by conventional casting, where the finite thermal diffusivity within the bulk material limits the final sample size of BMGs, denounced as critical casting thickness (CCT) [8]. The successful application of BMGs in PBF-LB/M has been reported for materials with a high

glass forming ability (GFA). Zr-based alloys, such as the ZR01 with a CCT of 12 mm [9–12], and alloys based on e.g. Pd, Fe, Al [13–15] are in the focus of current research. Those findings motivate an extension to materials with lower GFA such as the novel Ti-based sulfur-containing (TiS) BMGs [16]. In particular $Ti_{60}Zr_{15}Cu_{17}S_8$ exhibits a unique combination of desirable properties such as a flexural strength of 2.8 GPa, a low density of 5.5 g/cm³, a hardness of 547 HV5 and an exceptional corrosion resistance. Due to the low CCT of 1 mm, which limits the amorphous sample size to 1 mm, the applicability as a structural material is yet limited [5,16]. Prior work shows that the cooling rates theoretically exceed the critical limits for vitrification [4,17], however, the cyclic heating during PBF-LB/M affects the resulting microstructure, which may explain the reported process-induced cracking [18]. In this work, the laser power and scan speed are correlated with the resulting porosity, amorphous fraction, and hardness of $Ti_{60}Zr_{15}Cu_{17}S_8$. The results are critical in adressing the challenge of manufacturing amorphous, dense, and crack-free samples.

2 Methodology

2.1 Manufacturing of samples

A commercial PBF-LB/M machine of the type SLM280 HL 2.0 (Nikon SLM Solutions AG) was used to manufacture samples measuring 3 x 3 mm and a height of 10 layers from the atomized powder feed stock on a custom Ti grade 2 substrate. Arcal Prime Argon (99.998%, by Air Liquide) was used as shielding gas. The oxygen content within the atmosphere was controlled at 200 ppm by a Linde ADDVance O2 Precision device. If not specified otherwise, a layer thickness of 20 µm, a hatch distance of 70 µm and an alternating rotating scanning strategy (67° shift) are combined with three contour scans (50 W, 1600 mm/s). The scan speed v for the hatch and the laser power P are varied acc. to Table 1, based on previous work on Cu-Ti BMGs [19]. Based on preliminary experiments a pre-heating temperature of 423 K is applied to reduce in-situ cracking.

Table 1. Process parameters: Scan speed v and laser power P.

v	800 mm/s	1200 mm/s	1600 mm/s				
P	40 W	50 W	60 W	70 W	80 W	90 W	120 W

The variation of these parameters results in a wide range of the dimensionless normalized equivalent volume energy density E_0^* from 1.5 to 6.5, based on the work of Thomas et al. [20]:

$$E_0^* = \frac{A\,P}{2\,v\,l\,h\,\rho\,C_p\,(T_m - T_0)} \quad (1)$$

P = laser power
v = scan speed
l = layer thickness = 20 µm
h = hatch distance = 70 µm
A = absorptivity = 0.31 [17]
T_m = melting temperature = 1365 K [16]
T_0 = starting temperature = 423 K
C_p = heat capacity = 0.55 J/gK [17]
ρ = density = 5.5 g/cm³ [16]

2.2 Sample analysis

X-Ray diffraction (XRD) measurements are conducted using a Rigaku Smartlab High Resolution X-Ray diffractometer, equipped with a 9 kW rotating Cu-anode (wavelength 1.506 Å). Employing cross-beam optics results in a parallel X-Ray beam of 500 x 500 µm² size which is smaller than the surface of the 3 x 3 mm² samples. The positioning of the

samples into the full X-Ray beam is achieved by using a motorized scanning stage, confirmed by an on-top camera. From each of the individual samples, XRD patterns are recorded by $\theta - 2\theta$ scans in reflection geometry using a two-dimensional Hypix-3000 detector and azimuthally averaged, resulting into X-Ray diffractograms. At this X-Ray wavelength, and for an incident angle of θ = 45°, the attenuation length of the sample material is less than 8.5 µm. Thus, the XRD effectively probes the volume close to the sample surface. In order to remove any residual crystalline surface structures such as spatters [21], the measurements are performed on x-y surfaces after grinding with 280 grit grinding.

Subsequent sample polishing includes the following steps: Grinding with 220 to 1200 grain, polishing with 9 µm diamond suspension, and chemical polishing (50% MasterMet2, 40% distilled water, 10% hydrogen peroxide).

The relative density is measured based on the polished x-y microsections of the samples using an Olympus BX51 microscope combined with an Olympus SC50 digital camera and the Stream Essentials software.

The hardness of the samples is determined according to Vickers HV5. A Zwick Roell Type 3212 device is used on polished sample surfaces, executing 5 measurements per sample.

2.3 Data analysis

Several approaches have been described to analyze XRD data with respect to the determination of crystalline to amorphous material fractions [22,23]. For amorphous materials, lacking long-range translational order, a wide and halo-shaped scattering intensity can be expected, while crystalline material exhibits narrow but sharp Bragg reflections. For partially crystalline material, both an amorphous halo and crystalline reflections can be observed. This can be analyzed as a superposition of both signals [24]. The series of measurements is performed as follows: The samples are manufactured within a single process and the measurement of all samples is done within the same instrument, setup and series. The samples and data are thus subject to the same external influences. Based on the assumption that for this particular case the amorphous halo in the given data sets is approximately equal in area, intensity and position of its maximum, the approach of comparing the crystalline phase contribution of the registered intensity peak is applied. For this, after accounting for the background signal, the scattering signal from the amorphous phase is modelled as a Lorentzian ($y = y_0 + \left(2 \cdot \frac{A}{\pi}\right) \cdot (w/(4 \cdot (x - x_c)^2 + w^2))$, where x_c is the position of the maximum, w the width and A the area under the curve. The fit is iteratively applied with the chi² tolerance value of 10^{-9} to the range of $2\theta = 30°$ to 50°. The subtraction of this amorphous contribution from the experimental signal at the maximum intensity of the crystalline Bragg reflection is denoted as ΔI. This is used to quantify the crystallinity within the samples. A value of ΔI =0 represents an XRD amorphous sample. Thus, the influence of crystallinity on the hardness is investigated in this work.

3 Results and discussion

All samples are depicted in Figure 1: On the left side P = 40 W was used, and P increases towards the right side. The samples manufactured using P = 40 W, as well as the combination of P = 50 W and v = 1600 mm/s did not withstand the grinding and polishing process due to their high porosity. The combination of P = 50 W and 60 W with v = 800 mm/s results in a high density. In contrast, for v = 1200 mm/s in the middle row and v = 1600 mm/s in the bottom row, the samples exhibit an increase in porosity. The samples in Figure 1 have been subject to indentation hardness measurements. Samples manufactured with $E_0^* < 1.8$ did not achieve a required relative density of > 99.0% due to an inadequate energy input. In contrast,

manufacturing with $P > 80$ W resulted in a relative density > 99.9% in all combinations. In summary, as depicted in Figure 5, the density increases to approximately 100% and remains stable for $E_0^* > 2.7$.

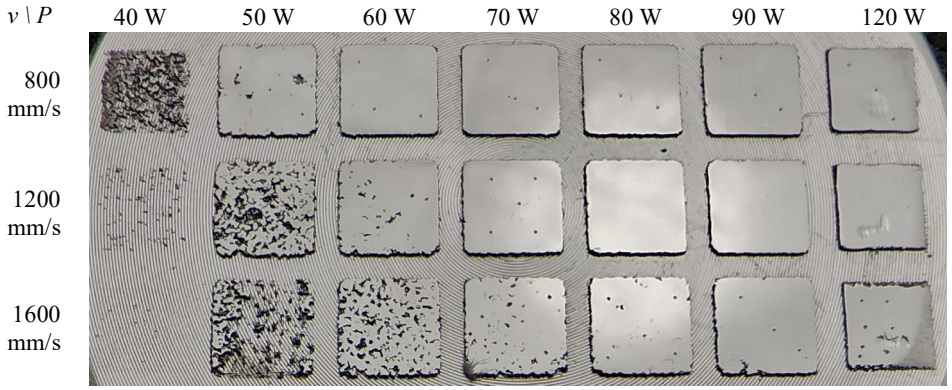

Figure 1. Manufactured 3x3 mm samples and corresponding process parameters.

The X-Ray diffractograms, exemplary shown in Figure 2 a) for samples processed with 1200 mm/s, reveal a partially crystalline microstructure in all samples. This is evidenced by the presence of an amorphous halo and a superposed crystalline reflection at an angle of $2\Theta = 37°$, corresponding to the Ti_2Cu phase, a Laves phase present in this alloy family, or a pure Ti phase [25]. However, the contribution of crystalline phases varies with laser power. The crystalline reflection is distinct at lower laser power of 40 W and decreases with increasing P until it reaches a minimum at 70 W. A further increase of P results in an augmented crystalline reflection. For the samples with the highest energy input of 120 W, additional reflections were observed at ~55°, which may relate to higher order crystalline reflections of the Ti phase within the sample or a signal originating from the displaced Ti base plate. The data obtained in this study are in good agreement with those reported by Kuball [16] for cast samples with a (partially) crystalline structure. However, a second reflection at approx. 42° was not observed in this work. In Figure 2 b) illustrates a Lorentzian curve, which indicates the superposition of the amorphous halo and the crystalline reflection. It is assumed that the contribution of the amorphous halo within the X-ray diffractogram is similar for all samples within this manufactured batch. Therefore, ΔI is used as a measure for crystallinity, as described in section 2.3. The results in dependence on E_0^* are presented in Figure 5 a).

The analysis of the powder feedstock indicates a high crystalline fraction within the powder feedstock material [18]. In light of these findings, it can be assumed that with a laser power of less than 50 W, the powder is not fully remolten, thereby preserving the crystalline microstructure. At medium energy input of $E_0^* = 2.25$ to 3.75 the powder is fully remolten, and the crystalline fraction is reduced, though not fully diminished. The potential of remelting crystalline powder into vitrified BMGs is also discussed by Barreto [26] and Deng [27]. At high energy input, an enhanced crystalline reflection is detected, indicating that the heat accumulation leads to crystallization. Two effects may occur: 1) due to the thermal cycling induced by multiple laser scan tracks within each layer and by application of multiple layers, the heat-affected zone (HAZ) of each scan track is subject to enhanced heat accumulation. This may lead to an extended period of time spend above the crystallization temperature, which could facilitate the formation and growth of crystals. 2) At high energy input and low heat dissipation within each scan track, the cooling time may be elongated, allowing for the formation of crystals, as demonstrated by Bruckhaus et al. [28]. In comparison with an X-

Ray diffractogram of the feedstock powder, the findings of this work support the hypothesis that cooling times during PFB-LB/M can be lower compared to those in atomization.

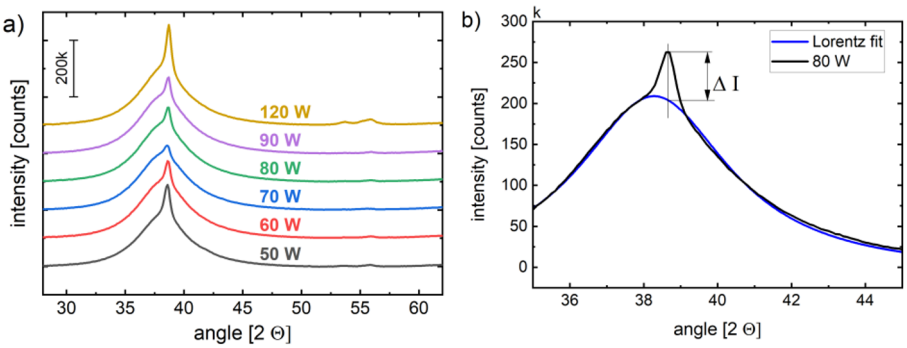

Figure 2. a) X-ray diffractograms of samples manufactured with 1200 mm/s b) measured XRD intensity (80 W – 1200 mm/s) and Lorentz based fit curve to approximate the amorphous halo and identify the contribution of the crystalline reflection as ΔI.

Since the amorphous structure of BMGs is a defining characteristic of their desirable properties, this study investigates the impact of the partial crystallinity on the hardness of the samples. The indents created during the measurement reveal two distinct failure modes: 1) toe formation of parallel cracks and 2) the initiation of cracks at the indent edges. Additionally, combinations of both modes and instances of plastic deformation can be observed. Two examples of parallel crack formation are depicted in Figure 3. In a), two cracks can be seen on the upper right quadrant. In b), the crack density is increased at the two left edges. In Figure 4, when the applied power exceeds 60 W, straight cracks emerge at the corners of the indents.

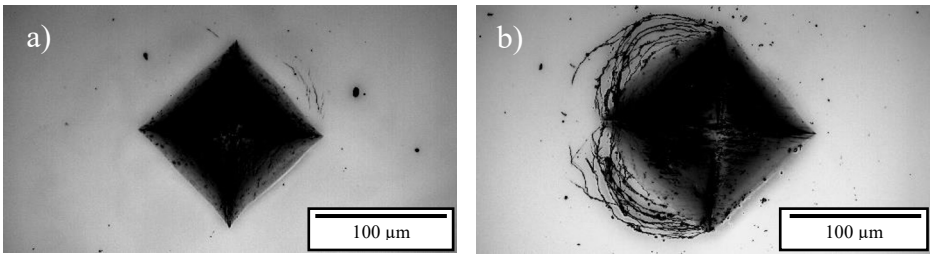

Figure 3. Hardness measurement indents. a) 70 W, 1200 mm/s with low crack density b) 120 W, 1600 mm/s with high crack density

Multiple defect appearances are present within a single sample. This indicates that no direct correlation to the microstructure or the process parameters can be estimated based on this study. Nevertheless, a discernible trend can be identified: an elevated energy input leads to an increase in crack length and branching. This hypothesis is corroborated by the images in Figure 4, which depict samples with v = 800 mm/s. At 50 W, shapes similar to shear bands can be seen, while at 60 to 90 W cracks of increasing length form. At 120 W, the formation of branched cracks was observed.

The formation of cracks and shear bands is reported for multiple BMGs and can be considered a typical deformation mechanism [29–31]. Therefore, their presence is consistent with the XRD measurements presented above, which indicate the existence of a partially crystalline and partially amorphous microstructure within the measured samples. The

mechanisms underlying the initiation and propagation of shear bands, as well as the plastic / elastic deformation of BMGs, remain a topic of ongoing research.

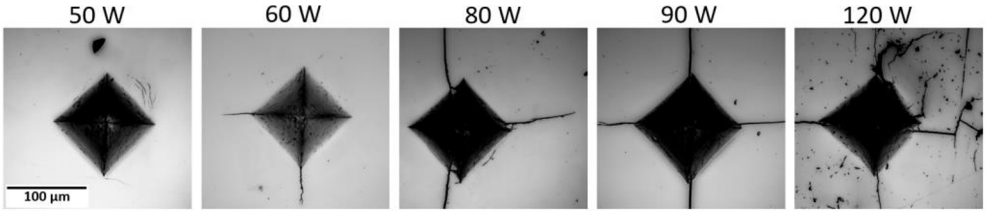

Figure 4. Hardness measurement indents for samples manufactured with 800 mm/s and increasing laser power.

To evaluate superposed peaks in the X-ray diffractograms, the amorphous contribution was fitted as described above. A corrected R^2 value of >0.98 was attained for all fitted curves. The measured hardness values and ΔI, which represents crystallinity, are presented in dependence on E_0^* in Figure 5 a). In the range of E_0^* between 2.25 and 3.75 the hardness value approaches ~ 537 ± 4 HV5, which is in close proximity to the reference value of 547 ± 6 HV5 for fully amorphous cast material (red line in Figure 5) [16]. At energy inputs of $E_0^* > 4$ the hardness decreases by up to 10% with increasing crystallinity. This correlation this correlation is not appliable to $E_0^* < 2$, where a pronounced reduction in hardness is not accompanied by an increasing crystallinity. Instead, as shown in Figure 5 b), the relative density reaches the minimum of 66.17% at the same point as the hardness. With increasing E_0^*, the relative density approaches 100% along with increasing hardness. Conversely, an increase in E_0^* does not result in a corresponding decrease in density within the investigated range.

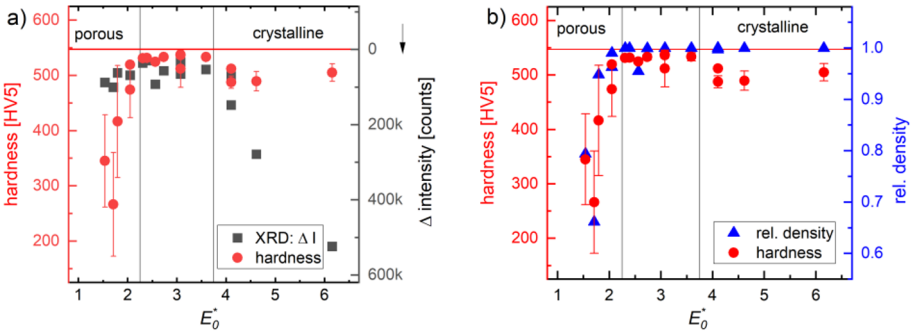

Figure 5. a) Hardness correlated to crystallinity, indicated by crystalline XRD peak contribution ΔI, plotted over the normalized line energy density E_0^*. b) hardness correlated to relative density plotted against E_0^*.

This allows the assumption, that the sample porosity limits the mechanical performance when confronted with a low energy input during manufacturing. On the other hand, a high density does not necessarily imply a high hardness, and recrystallization appears to be the primary limiting factor with regard to high energy input. When interpreting the results in combination with the images of the hardness indents, it can be assumed that the decrease of hardness is linked to an increasingly brittle material that is unable to withstand the rigors of a hardness measurement. The decrease in hardness at $E_0^* > 4$ relates to cracked hardness indents rather than a "soft" material. This brittle material is not suitable for manufacturing since tensions induced by thermal cycling cannot be accounted for. Thus, three regimes are separated in the graphs in Figure 5: in the first regime at $E_0^* < 2.25$, porosity represents the

limiting factor. In the range above 3.75, recrystallization represents the limiting factor. In the intermediate range, where a high density and optimized amorphicity are combined, a high hardness is observed. Accordingly, a range of favorable processing parameters is identified between E_0^* values of 2.25 to 3.75. For purposes of comparison: Thomas et al. [20] calculated values of $E_0^* = 2$ to 9 for the dense manufacturing of the crystalline, well-known alloy Ti64. The range for manufacturing is thus within the same range, however, it is restricted by the needed prevention of crystallization. Wegner [32] determined the processing window for two glass-forming alloys: $E_0^* = 1.8$ to 2.3 for Cu-Ti-based Vit101 and $E_0^* = 2$ to 4 for Zr-based ZR01. The determined values for $Ti_{60}Zr_{15}Cu_{17}S_8$ are reasonable and can be utilized for further research on the optimization of process parameters.

4 Conclusion

It is found that by an adequate choice of laser power and scan speed the degree of crystallinity in additively manufactured $Ti_{60}Zr_{15}Cu_{17}S_8$, although not vanishing, can be significantly reduced. Thereby a hardness of 537 HV5 is reached, which approaches 547 HV5 of fully amorphous material [16]. Porosity and reduced hardness linked to insufficient energy input of less than 50 W is reported. An increasing crystallinity related to excessive laser power is found to reduce the hardness by 10%. This correlation may also apply to other mechanical properties that depend on the microstructure, such as fracture strength and elastic strain. For further research the favorable energy input range of $E_0^* = 2.25$ to 3.75 leading to dense and optimized amorphous samples is provided by this study. The influence of process parameters on the plasticity and elasticity are yet to be investigated.

This research was funded by the German Research Foundation (DFG) through Grant No. KL 3357/1-1. The funded instruments are: SLM 280 HL (PBF-LB/M system) by DFG Grant No. INST 20876/341-1 as well as the Rigaku Smartlab High Resolution X-ray diffractometer of the Nanoparticle Processing Technology (NPPT) group by DFG INST 20876/395-1 FUGG and the state of North Rhine-Westphalia, Germany. We would like to thank Tobias Deckers and Pierre Foret (Linde AG) for providing the ADDVance O2 precision system. Further, we thank Prof. Stefanie Hanke and Dajana Valenta for fruitful discussions and support in metallographic and hardness analysis. We acknowledge support from the Open Access Publication Fund of the University of Duisburg-Essen.

References

[1] T. Wohlers, R.I. Campbell, O. Diegel, R. Huff, J. Kowen, Wohlers report 2024: Analysis. Trends. Forecasts. 3D Printing and Additive Manufacturing State of the Industry, 2024.

[2] P. Köhnen, M. Létang, M. Voshage, J.H. Schleifenbaum, C. Haase, Understanding the process-microstructure correlations for tailoring the mechanical properties of L-PBF produced austenitic advanced high strength steel, Additive Manufacturing 30 (2019) 100914. https://doi.org/10.1016/j.addma.2019.100914.

[3] W.E. Frazier, Metal Additive Manufacturing: A Review, J. of Materi Eng and Perform 23 (2014) 1917–1928. https://doi.org/10.1007/s11665-014-0958-z.

[4] S. Pauly, P. Wang, U. Kühn, K. Kosiba, Experimental determination of cooling rates in selectively laser-melted eutectic Al-33Cu, Additive Manufacturing 22 (2018) 753–757. https://doi.org/10.1016/j.addma.2018.05.034.

[5] C. Suryanarayana, A. INOUE, Bulk Metallic Glasses, Second Edition, secondnd ed., CRC Press, Milton, 2017.

[6] N. Sohrabi, J. Jhabvala, R.E. Logé, Additive Manufacturing of Bulk Metallic Glasses—Process, Challenges and Properties: A Review, Metals 11 (2021) 1279. https://doi.org/10.3390/met11081279.
[7] F.E. Luborsky (Ed.), Amorphous metallic alloys, Butterworths, London, Boston, 1983.
[8] R. Busch, J. Schroers, W.H. Wang, Thermodynamics and Kinetics of Bulk Metallic Glass, MRS Bull. 32 (2007) 620–623. https://doi.org/10.1557/mrs2007.122.
[9] J. Wegner, M. Frey, R. Busch, S. Kleszczynski, Additive manufacturing of a compliant mechanism using Zr-based bulk metallic glass, Additive Manufacturing Letters 39 (2021) 100019. https://doi.org/10.1016/j.addlet.2021.100019.
[10] P. Bordeenithikasem, M. Stolpe, A. Elsen, D.C. Hofmann, Glass forming ability, flexural strength, and wear properties of additively manufactured Zr-based bulk metallic glasses produced through laser powder bed fusion, Additive Manufacturing 21 (2018) 312–317. https://doi.org/10.1016/j.addma.2018.03.023.
[11] S. Pauly, C. Schricker, S. Scudino, L. Deng, U. Kühn, Processing a glass-forming Zr-based alloy by selective laser melting, Materials & Design 135 (2017) 133–141. https://doi.org/10.1016/j.matdes.2017.08.070.
[12] N. Luo, F. Galgon, S. Krauß, L.A. Morales, B. Merle, C.H. Zenk, C. Körner, Microstructural evolution and mechanical properties in Zr–Cu–Al–Nb bulk metallic glass composites prepared by laser metal deposition, Intermetallics 140 (2022) 107393. https://doi.org/10.1016/j.intermet.2021.107393.
[13] N. Sohrabi, J. Jhabvala, G. Kurtuldu, R. Frison, A. Parrilli, M. Stoica, A. Neels, J.F. Löffler, R.E. Logé, Additive manufacturing of a precious bulk metallic glass, Applied Materials Today 24 (2021) 101080. https://doi.org/10.1016/j.apmt.2021.101080.
[14] X.P. Li, M. Roberts, Y.J. Liu, C.W. Kang, H. Huang, T.B. Sercombe, Effect of substrate temperature on the interface bond between support and substrate during selective laser melting of Al–Ni–Y–Co–La metallic glass, Materials & Design (1980-2015) 65 (2015) 1–6. https://doi.org/10.1016/j.matdes.2014.08.065.
[15] Di Ouyang, W. Xing, N. Li, Y. Li, L. Liu, Structural evolutions in 3D-printed Fe-based metallic glass fabricated by selective laser melting, Additive Manufacturing 23 (2018) 246–252. https://doi.org/10.1016/j.addma.2018.08.020.
[16] A. Kuball, O. Gross, B. Bochtler, B. Adam, L. Ruschel, M. Zamanzade, R. Busch, Development and characterization of titanium-based bulk metallic glasses, Journal of Alloys and Compounds 790 (2019) 337–346. https://doi.org/10.1016/j.jallcom.2019.03.001.
[17] H. Schönrath, J. Wegner, M. Frey, E. Soares Barreto, A. Elspaß, N. Schnell, B. H. R. Erdmann, J. Neises, N. Ellendt, R. Busch, S. Kleszczynski, Analytical Modeling of Cooling Rates in PBF-LB/M of Bulk Metallic Glasses, in: SFF Symposium Preceedings 2023.
[18] H. Schönrath, J. Wegner, M. Frey, M.A. Schroer, X. Jin, M.T. Pérez-Prado, R. Busch, S. Kleszczynski, Novel titanium-based sulfur-containing BMG for PBF-LB/M, Prog Addit Manuf 9 (2024) 601–612. https://doi.org/10.1007/s40964-024-00668-z.
[19] M. Frey, J. Wegner, E.S. Barreto, L. Ruschel, N. Neuber, B. Adam, S.S. Riegler, H.-R. Jiang, G. Witt, N. Ellendt, V. Uhlenwinkel, S. Kleszczynski, R. Busch, Laser powder bed fusion of Cu-Ti-Zr-Ni bulk metallic glasses in the Vit101 alloy system, Additive Manufacturing 66 (2023) 103467. https://doi.org/10.1016/j.addma.2023.103467.
[20] M. Thomas, G.J. Baxter, I. Todd, Normalised model-based processing diagrams for additive layer manufacture of engineering alloys, Acta Materialia 108 (2016) 26–35. https://doi.org/10.1016/j.actamat.2016.02.025.

[21] J. Wegner, L. Bruckhaus, M.A. Schroer, M. Rayer, H. Schoenrath, S. Kleszczynski, Zr-based bulk metallic glasses in PBF-LB/M: near-polished surface quality in the as-built state, Prog Addit Manuf 9 (2024) 585–591. https://doi.org/10.1007/s40964-024-00667-0.
[22] G. Korösy, K. Tomolya, D. Janovszky, J. Sólyom, Evaluation of XRD Analysis of Amorphous Alloys, MSF 729 (2012) 419–423. https://doi.org/10.4028/www.scientific.net/MSF.729.419.
[23] B. Shah, V.K. Kakumanu, A.K. Bansal, Analytical techniques for quantification of amorphous/crystalline phases in pharmaceutical solids, J. Pharm. Sci. 95 (2006) 1641–1665. https://doi.org/10.1002/jps.20644.
[24] L.M. Moreau, D.-H. Ha, H. Zhang, R. Hovden, D.A. Muller, R.D. Robinson, Defining Crystalline/Amorphous Phases of Nanoparticles through X-ray Absorption Spectroscopy and X-ray Diffraction: The Case of Nickel Phosphide, Chem. Mater. 25 (2013) 2394–2403. https://doi.org/10.1021/cm303490y.
[25] L.M. Ruschel, B. Adam, O. Gross, N. Neuber, M. Frey, H.-J. Wachter, R. Busch, Development and optimization of novel sulfur-containing Ti-based bulk metallic glasses and the correlation between primarily crystallizing phases, thermal stability and mechanical properties, Journal of Alloys and Compounds 960 (2023) 170614. https://doi.org/10.1016/j.jallcom.2023.170614.
[26] E. Soares Barreto, M. Frey, J. Wegner, A. Jose, N. Neuber, R. Busch, S. Kleszczynski, L. Mädler, V. Uhlenwinkel, Properties of gas-atomized Cu-Ti-based metallic glass powders for additive manufacturing, Materials & Design 215 (2022) 110519. https://doi.org/10.1016/j.matdes.2022.110519.
[27] L. Deng, S. Wang, P. Wang, U. Kühn, S. Pauly, Selective laser melting of a Ti-based bulk metallic glass, Materials letters 212 (2018) 346–349. https://doi.org/10.1016/j.matlet.2017.10.130.
[28] L. Bruckhaus, J. Wegner, N. Schnell, H. Schönrath, E.S. Barreto, N. Ellendt, M. Frey, R. Busch, S. Kleszczynski, Empirical calibration method for the thermal simulation of Cu47Ti34Zr11Ni8 single tracks in laser powder bed fusion: Science forum Rapid.Tech 3D 2024, Progress in Additive Manufacturing 9 (2024). https://doi.org/10.1007/s40964-024-00653-6.
[29] G. Subhash, H. Zhang, Shear Band Patterns in Metallic Glasses under Static Indentation, Dynamic Indentation, and Scratch Processes, Metall Mater Trans A 38 (2007) 2936–2942. https://doi.org/10.1007/s11661-007-9315-2.
[30] J.F. Löffler, Bulk metallic glasses, Intermetallics 11 (2003) 529–540. https://doi.org/10.1016/S0966-9795(03)00046-3.
[31] C. Schuh, T. Hufnagel, U. Ramamurty, Mechanical behavior of amorphous alloys, Acta Materialia 55 (2007) 4067–4109. https://doi.org/10.1016/j.actamat.2007.01.052.
[32] Jan Wegner, Funktionalisierung der prozessinhärenten Abkühlraten des Laser-Strahlschmelzens zur Verarbeitung metallischer Massivgläser, Duisburg, 2023.